Thermal Analysis of Buried Land Mines Over a Diurnal Cycle

Khalil Khanafer and Kambiz Vafai

***Abstract*—The passive infrared (IR) imaging signature of buried mines under three different soil surface conditions is investigated in this work. The three-dimensional (3-D) nature of the mine, the site, and the temporal attributes of surrounding climate and exposed radiation are accounted for large and moderate-scale clutter surfaces as well as a smooth surface. The effect of the short- and long-wavelength radiation as well as the convective heat transfer is incorporated in this analysis and the temporal development of the temperature distribution over a diurnal cycle is presented for different surface conditions. The occurrence of false alarm mine spots is demonstrated using the moderate scale clutter surface and a critical period of time for the landmine signature is established for different soil surface conditions. The present results show that mines buried at moderate depths in the soil would not produce a direct signature.**

***Index Terms*—Buried mines, false alarm mine spots, infrared imagining signature, shallow and moderate depth mines, surface roughness.**

I. Introduction

DEMINING processes are generally slow, expensive, manpower-intensive, and suffer from high false alarm rates. Current mine detection methods vary from simple manual probing to a variety of high-tech electronic schemes, chemical, and biological detection methods. Examples include magnetic resonance imaging, infrared (IR), thermal images, thermal neutron activation (TNA), acoustic sensors, and ground-penetrating radar, to name just a few.

Infrared mine detection is a promising technique in the detection and discrimination of the landmines from other buried objects based on the knowledge of the physical properties of land mines and the soil containing the mines. A buried mine can be detected if its thermal signature exists on the soil surface. The landmine signatures are controlled essentially by the environmental conditions and the differences in the thermo-physical properties of the soil and the mine, respectively. The lack of knowledge of the landmine signature may result in improper performance of the mine detection system. Due to the differences in the physical properties of the soil and the mine, a thermal contrast exists above the mine and consequently, IR cameras can be used successfully to capture the changes in temperatures over the mine.

Buried landmine detection using IR imaging technology is a subject of interest by many researchers. Most of the researchers have focused their attention toward the development of the signal processing algorithms and the associated performance of the sensors while ignoring several pertinent effects such as solar heating, soil disturbances, and temporal climate variations. Better knowledge of these effects on the landmine signature is required to properly use demining IR sensors and to interpret IR imagery.

Reference [1] investigated the influence of the emissivity on the signatures of a specific target in the context of their two-color IR system. The time development for both buried and surface mines using several sensors is examined by [2]. Their results showed that the surface laid targets are visible during the whole diurnal cycle while the buried targets are only visible during sunrise and sunset. A similar study is conducted by [3] to measure the temperatures of both live and substitute mines through multiple diurnal cycles. Reference [4] investigated experimentally a systematic approach to improve landmine detection capability using passive IR imaging camera. Polarization-sensitive IR sensing is also used to assist distinguishing between a man-made object and the background [5], [6]. Reference [7] used a preprocessing algorithm dedicated to polarimetric IR imager in order to help the discrimination between natural and man made objects. Reference [8] presented spectroscopic data collected by a nonimaging sensor.

Reference [9] conducted an experimental work for surface land mine detection. They used polarization-sensitive IR sensing to highlight the polarization signature of man-made targets such as land mines over natural features in the image. Fuzzy rule-based fusion technique on the processed polarization resolved image was used to reduce the number of false alarms. Another work related to this area is by [10]. A three-dimensional (3-D) dynamic thermal imaging of structural flaws using dual-band IR computed tomography is analyzed in this study. The measurements out of this study are compared well with calculations based on a 3-D finite element thermal model (TOPAX3D).

The enhancement of thermal landmine signatures using IR sensors was investigated experimentally by [11]. They used microwave energy source to penetrate the soil and to provide a volumetric heating of the site. In their investigation, they presented a one-dimensional (1-D) model of microwave absorption and heat dissipation by moisture-laden soils, which contain landmine-like buried objects. Detection of antipersonnel landmines based on water-jet induced thermal images was studied experimentally by [12]. They used an array of heated water-jets to rapidly induce a thermal signature of buried objects in the region of interest. Consequently, a temperature profile on the soil surface is formed due to conduction and radiation heat transfer

Manuscript received July 20, 2000; revised October 4, 2001.

K. Khanafer is with the Department of Mechanical Engineering, The Ohio State University, Columbus, OH 43210 USA.

K. Vafai is with the Department of Mechanical Engineering, University of California, Riverside, CA 92521 USA (e-mail: vafai@engr.ucr.edu).

Publisher Item Identifier S 0196-2892(02)01876-4.

from the water blocked and reflected by the surface of the buried object and the heating of the object itself due to the heat transferred from the water-jet. The time history of the soil surface temperature is obtained using IR after the water-jets are applied.

A generalized model on the effect of the buried landmines on the soil temperature over a diurnal cycle is not well-established in the literature. Only a few preliminary theoretical studies have been conducted in this area similar to the analysis by [13], which is drawn from a classical solution [14]. References [15]–[17] conducted a study in the absence of the mine for a 1-D model in which the temperature depends only on the depth from the soil surface. Recently, Baertlin *et al.* [18] conducted a preliminary 3-D study to illustrate the effect of the buried landmines on the surface temperature distribution. In this study, they showed that the effect of the landmines on the structure of the soil's temperature could not be obtained using a 1-D model due to the 3-D heat transfer through the soil and the mine. However, several pertinent effects were ignored in their study.

The objective of the present work is to develop a 3-D thermal model for soil containing the buried landmine over a diurnal cycle and accounting for the surface roughness. This model will help improve the performance of thermal IR imagery and lead to the development of more robust signal processing techniques. Simulant anti-tank mine will be used in the present investigation. Most mines normally have a few very small components. Such components include the insert which represents the mine's striker mechanism to initiate the explosion. Since the insert is composed of different physical properties than the TNT material, the effect of the insert on the soil temperature distribution also will be included in this analysis.

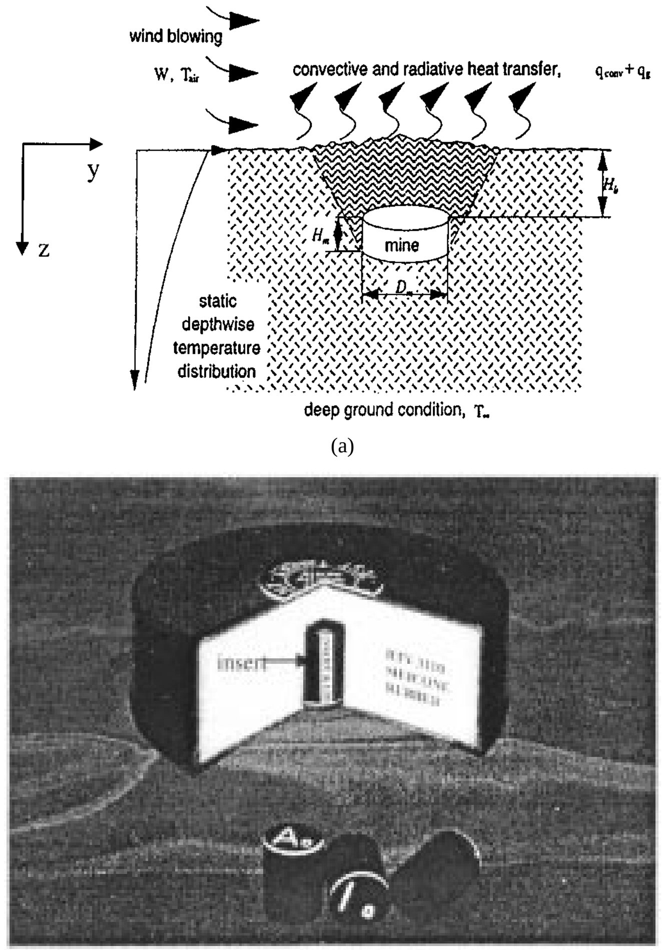

Fig. 1. (a) Schematic diagram of the problem and (b) model of the simulant anti-tank mine used in this investigation.

II. Mathematical Formulation

A. Governing Equations

In this work, single-phase 3-D transient heat conduction equations for the soil and mine are utilized. The soil and mine are modeled as isotropic solids. A surrogate anti-tank mine buried beneath the soil is used in this simulation as shown in Fig. 1 and 2. Assuming that the temporal variation of the moisture content is negligible, the resulting governing equations for the soil, insert, and the mine can be written as follows:

for soil:
$$\frac{\partial}{\partial t}(\rho c T)_s = \nabla(k\nabla T)_s \tag{1}$$
for the insert:
$$\frac{\partial}{\partial t}(\rho c T)_I = \nabla(k\nabla T)_I \tag{2}$$
for TNT:
$$\frac{\partial}{\partial t}(\rho c T)_m = \nabla(k\nabla T)_m \tag{3}$$

where ρ, c, k, and T are the density, specific heat, thermal conductivity, and temperature respectively. The subscripts, s, I, and m denote the soil, insert, and the mine, respectively. The boundary conditions for the afore-mentioned equations can be summarized as follows:

1) at the soil surface:
$$\overrightarrow{n}.k_s\nabla T_s = q_{net} \tag{4}$$

2) at the insert surface:
$$\overrightarrow{n}.k_I\nabla T_I = \overrightarrow{n}.k_m\nabla T_m \tag{5}$$

3) at the mine surface:
$$\overrightarrow{n}.k_s\nabla T_s = \overrightarrow{n}.k_m\nabla T_m \tag{6}$$

4) at the deep soil below the mine:
$$T_s \rightarrow T_\infty \tag{7}$$

where $\overrightarrow{n}$ represents the normal unit vector, T_∞ is the deep soil temperature below the buried mine, and q_{net} is the net heat flux into the top surface of the soil and is given by the following expression:
$$q_{net} = q_{conv} + q_{sun} + q_{sky} - q_{emis} - q_{evap} \tag{8}$$

where q_{con} is the convective heat transfer between the surface of the soil and the atmosphere, q_{sun} is the incident solar energy reduced by cloud cover, atmospheric absorption, albedo, and the cosine of the zenith angle. The sky brightness with a small correction for cloud cover is represented by q_{sky}, q_{emis} is the gray body emission from the soil's surface and q_{evap} is the latent cooling of the ground caused by evapotranspiration and

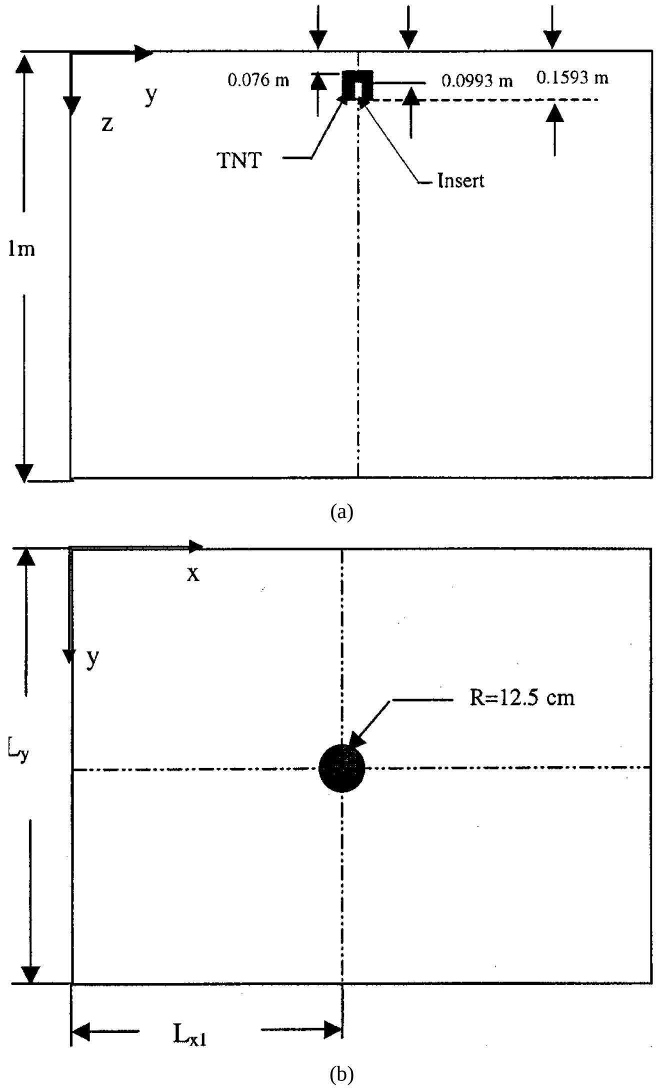

Fig. 2. (a) Sectional view of the TNT and insert objects and (b) top view of the mine object ($L_y = 2L_{x1} = 2m$).

condensation. In this investigation, the soil is assumed to be dry and therefore q_{evap} is set to zero in this model. Convective heat transfer between the soil and the surrounding air is given by

$$q_{conv} = Ah(T_{air} - T_s) \tag{9}$$

where h is the convective heat transfer coefficient ($h = 5$ W/m^2 K based on the typical average wind speed of 2 m/s) and A is the exposure surface area. A general ambient temperature variation is imposed as

$$T_{air} = 293 - 5\cos\left(\frac{2\pi(t-2)}{24}\right) \tag{10}$$

where t is given in hours (starting from midnight). The sky irradiance based on the long-wavelength radiation downward from the atmosphere can be expressed as

$$q_{sky} = \sigma\varepsilon A T_{sky}^4 \tag{11}$$

where $\sigma = 5.67 \times 10^{-8}$ W/m^{2}K^4 is the Stephan–Boltzman constant, ε is the mean emissivity of the surface, and T_{sky} is the effective sky radiance temperature given by

$$T_{sky} = 0.9 \times T_{air}. \tag{12}$$

The long-wave radiation emission from the ground's surface is given by the following equation:

$$q_{emis} = \sigma\varepsilon A T_s^4 \tag{13}$$

where T_s is the soil's surface temperature.

The short-wavelength incident solar radiation can be expressed as follows:

$$q_{sun} = (1 - C_L)S_o(1 - C)M(\phi)\cos(\phi) \tag{14}$$

where $C_L(=0.2)$ is the cloud cover, $C(=0.3)$ is the ground albedo, and $S_o(=1385$ W/m$^2)$ is the solar constant. $M(\phi)$ is the approximate atmospheric transmissivity and is given as [19]

$$M(\phi) = 1 - 0.2\cos(\phi)^{-0.5} \tag{15}$$

where ϕ is the zenith angle and can be determined from the following expression

$$\cos(\phi) = \begin{pmatrix} \cos\lambda\cos\delta\left(-\cos\left(\frac{2\pi t(h)}{24}\right) + \sin\lambda\sin\delta\right), \\ \text{if } > 0 \\ \text{otherwise,} \quad \cos(\phi) = 0 \end{pmatrix} \tag{16}$$

where λ is the local latitude $(=45^\circ)$ and δ is the declination given by

$$\delta = -23.43^\circ \cos\left(\frac{2\pi \text{ month}}{12}\right). \tag{17}$$

The initial condition for (1)–(3) corresponds to typical conditions and is given as

$$T_s = T_m = T_I = 293K. \tag{18}$$

B. Rough Surface Approximation

In general, the soil is not smooth and has variations in different directions. These variations should be taken into consideration due to their significant effects on the mine signature and consequently the performance of IR sensors. Ignoring the effect of the surface fluctuations may result in false alarm by IR sensors. As such, the top surface of the soil is represented by couple of generic rough surface models. Three types of surface conditions will be used for our study; namely the sloping rough surface, the periodically rough surface, and the smooth surface.

1) Sloping Surface Description (Large Scale Clutter): A generic rough surface is constructed with a full-cycle sine in the x-direction and a half-cycle cosine in the y-direction as follows:

$$z(x, y) = A\sin(\pi x/L_{x1})\cos(\pi y/2L_{y1}) \tag{19}$$

where A (=1.5 cm) is the amplitude of the surface variation about the mean and L_{x1} and L_{y1} are the x and y dimensions. For $L_{x1} = L_{y1} = 1$ m, this will produce a surface having a 3-cm

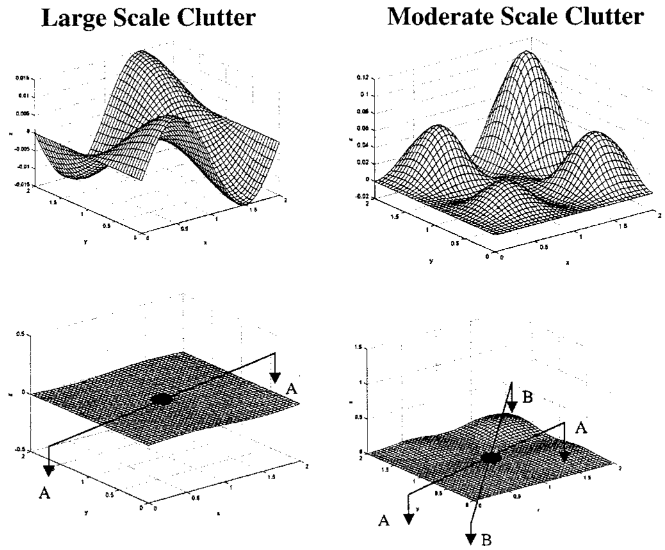

Fig. 3. (a) Sloping rough surface and (b) periodically rough surface.

peak-to-peak variation. This surface goes smoothly to zero at the edges, so assumptions of periodic boundary conditions in x and y directions will not produce any surface discontinuities. A sketch of the sloping rough surface is shown in Fig. 3(a).

2) Periodically Rough Surface (Moderate Scale Clutter): In this part a generic surface that has a flat area in the center and some "bumps" away from the center is utilized. A generic form of such variation is given by

$$\begin{aligned} z =& 0.15\cos[\pi x/(2L_{x1})]\cos[\pi y/(2L_{y1})] \\ &\times \sin[\pi(1-\cos(\pi x B/L_{x1}))] \\ &\times \sin[\pi(1-\cos(\pi y B/L_{y1}))] \end{aligned} \tag{20}$$

where B is a user-defined parameter and L_x and L_y are the correlation lengths in the x and y directions respectively. In this work, $L_{x1} = L_{y1} = 1$m. This expression produces zero surface slope in the center and symmetrically placed bumps. For $B = 0.4$, we obtain four bumps (one in each quadrant). The surface also goes smoothly to zero at each of the boundaries. The rough surface constructed by (20) is shown in Fig. 3(b).

III. Numerical Scheme

A Galerkin-based FEM is employed to solve the governing equations for the present study. The application of this procedure is well documented [20]. The segregated solution algorithm is utilized to solve the system of equations. The advantage of using this method is that the global system matrix is decomposed into smaller submatrices and then solved in a sequential manner. This technique will result in considerably fewer storage requirements. Extensive numerical experimentation was performed to attain grid-independent results for all the field variables. Variable time step was implemented successfully in this model without any loss in the accuracy of the results. One diurnal cycle (24 h) was found to take about 36 h on an SGI Octane Workstation. This was necessary to increase the accuracy of the present results.

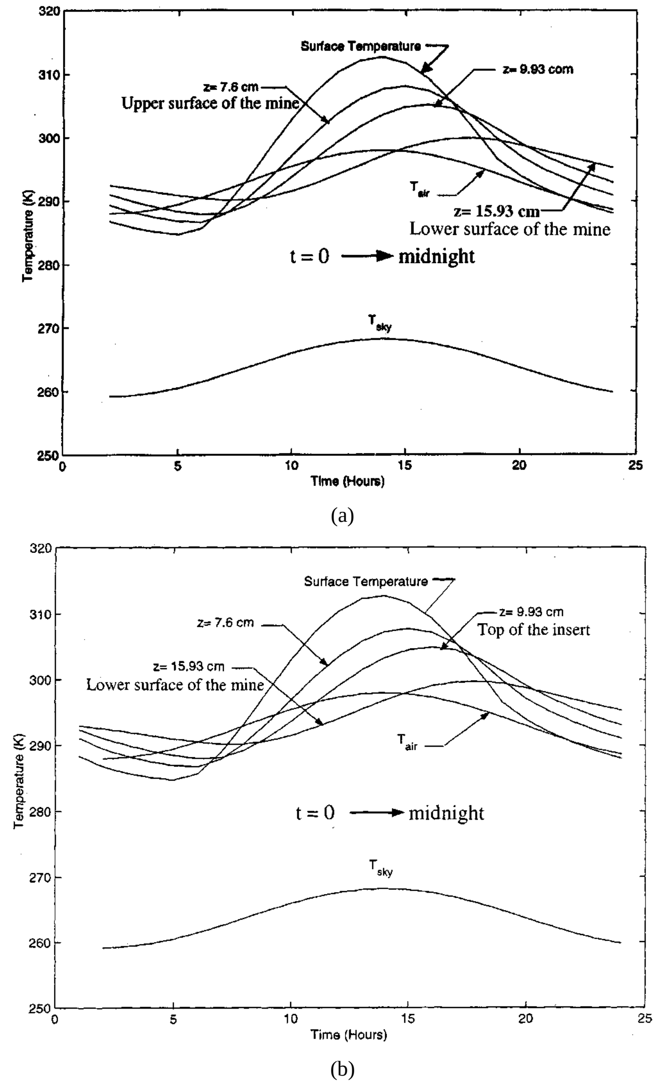

Fig. 4. Comparison between the ambient temperature and the temporal variation of the soil average temperature at various depths (a) large-scale clutter surface and (b) moderate-scale clutter surface.

TABLE I
SPECIFICATION OF TNT

Mine Type	D mm	H mm	k W/m.K	c J/kg.K	ρ kg/m³
Anti-Tank	250	83.3	0.223442	1289.29	1560

TABLE II
SPECIFICATION OF THE INSERT MATERIAL

D mm	H mm	k W/m.K	c J/kg. K	ρ kg/m³
40	60	0.0263	1007	1.164

TABLE III
SPECIFICATION OF THE SOIL (SANDY GRAVEL)

k W/m.K	c J/kg. K	ρ kg/m³
2.5116	837.2	2000

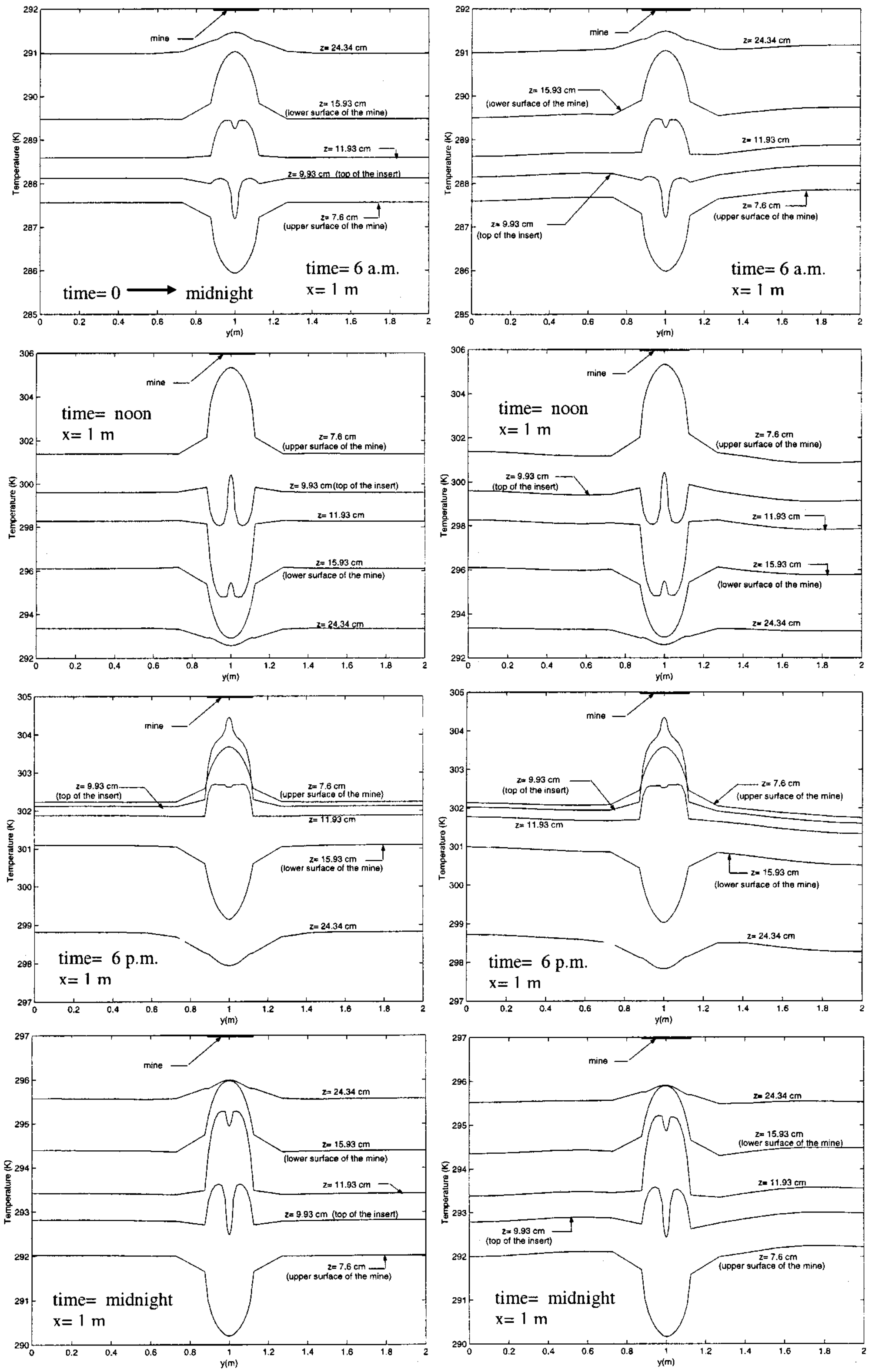

(a) (b)

Fig. 5. Temporal variation of the temperature at various depths of the soil (a) large scale clutter surface and (b) moderate scale clutter surface.

IV. Discussion of Results

As we mentioned previously, three basic types of surfaces are investigated to illustrate their impact on the mine signature. These are composed of a smooth surface and two generic models of the rough soil surfaces. A simulant anti-tank mine buried at 7.6 cm beneath the soil is used in this simulation as shown in Fig. 1. The mine is modeled as an object of circular shape having the same thermal properties as that of TNT. Typical dimensions of the mine and the insert are used in this investigation as shown

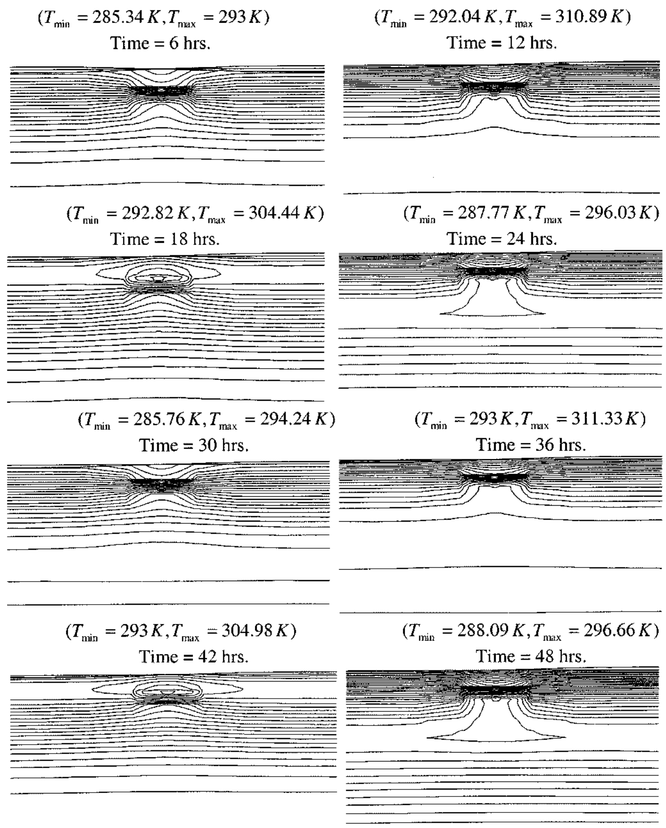

Fig. 6. Effect of the presence of the mine on the depth-wise temperature distribution (plane A–A) at various times (every 6 h) for large scale clutter surface; t = 6–48 h.

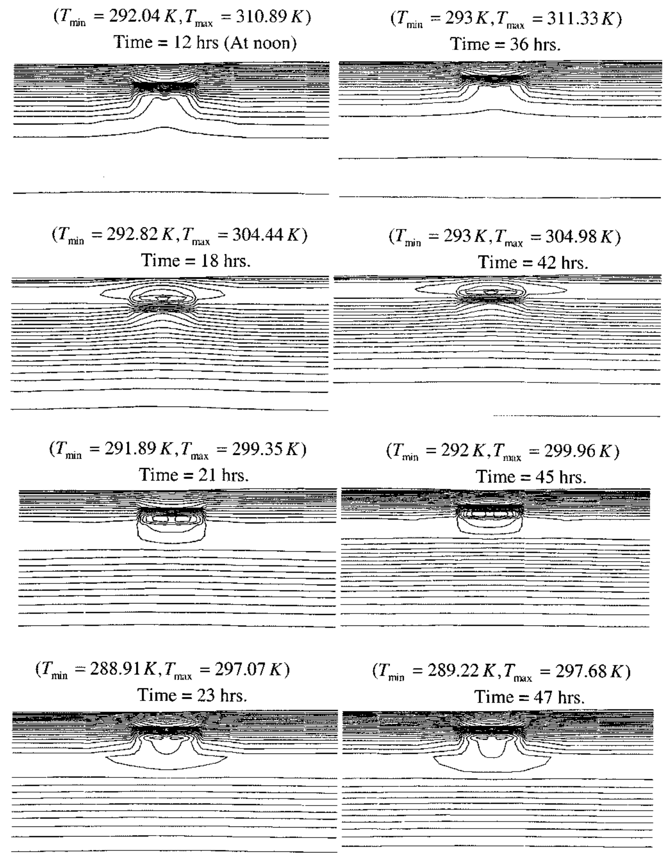

Fig. 7. Periodicity of the depth-wise temperature distribution (plane A–A) at various periods of time for an anti-tank simulant buried at 7.6 cm beneath a large-scale clutter surface; t = 12, 18, 21, and 23 h, respectively.

in Fig. 2. The thermophysical properties of the soil, insert, and the anti-tank mine are tabulated in Tables I–III. The two sections (AA and BB) in Fig. 3 will be used in later figures to present the temperature distribution at these sections. For large- and moderate-scale clutter cases, Fig. 4 shows a comparison of the soil average temperature at various depths. It is qualitatively seen in Fig. 4, as illustrated by the contour curvature variations, that the temperature of the surface of the soil as well as the variations at different depths incorporate the ambient and sky temperature variations.

The effect of the presence of the mine on the temperature of the soil at different sections and periods of time is clearly shown in Fig. 5 for large and moderate scale clutter surfaces. Fig. 5 shows that the surface temperature over the mine is cooler than the surface temperature beneath the mine 6 h after midnight. This can be attributed to the fact that the mine tends to resist the conduction heat transfer through the soil as a result of its lower thermal conductivity as compared to the soil thermal conductivity. Moreover, the incoming short-wavelength radiation from the sun depends on the sunset and sunrise times and for this period of time, this effect is negligible resulting in a cooler mine surface at dawn. Furthermore, higher radiation heat loss from the surface to the surrounding is occurring until the sunrise resulting in a lower temperature above the mine. As time proceeds (after 12 h), Fig. 5 shows that the temperature distribution pattern reverses in such way that the temperature of the soil over the mine becomes hotter than the surface beneath the mine. This result is due to two competing effects, the short-wavelength absorbed solar energy and the long-wavelength radiation loss into the sky.

Over the period of 18 to 24 h, more heat is absorbed by the mine causing the insert to become hotter than the surrounding due to its smaller thermal conductivity as seen in Fig. 5. During the night, the mine tends to block the upward heat transfer by conduction through the soil and allows downward heat transfer and as a result, the area of the soil above the mine becomes cooler. In addition, the weak effect of the short-wavelength radiation from the sun during this period of time leads to lower temperatures above the mine.

Fig. 5 also shows that the insert within the mine has a significant effect on the soil depth-wise temperature distribution due to different physical properties of the media surrounding the insert. This sudden variation in the temperature is clearly shown only along the top surface of the insert. This trend of reversal in the temperature pattern can lead to an improvement in the mine detection method such as IR imaging method while neglecting this effect can lead to substantial errors.

The effect of the buried mine on the depth-wise temperature distribution over two complete diurnal cycles starting six h after midnight for large-scale clutter surface is observed in Fig. 6. This figure provides a vivid picture of the effect of the mine on the soil depth-wise temperature at various periods of time. The isotherms around the insert are split identically due to the

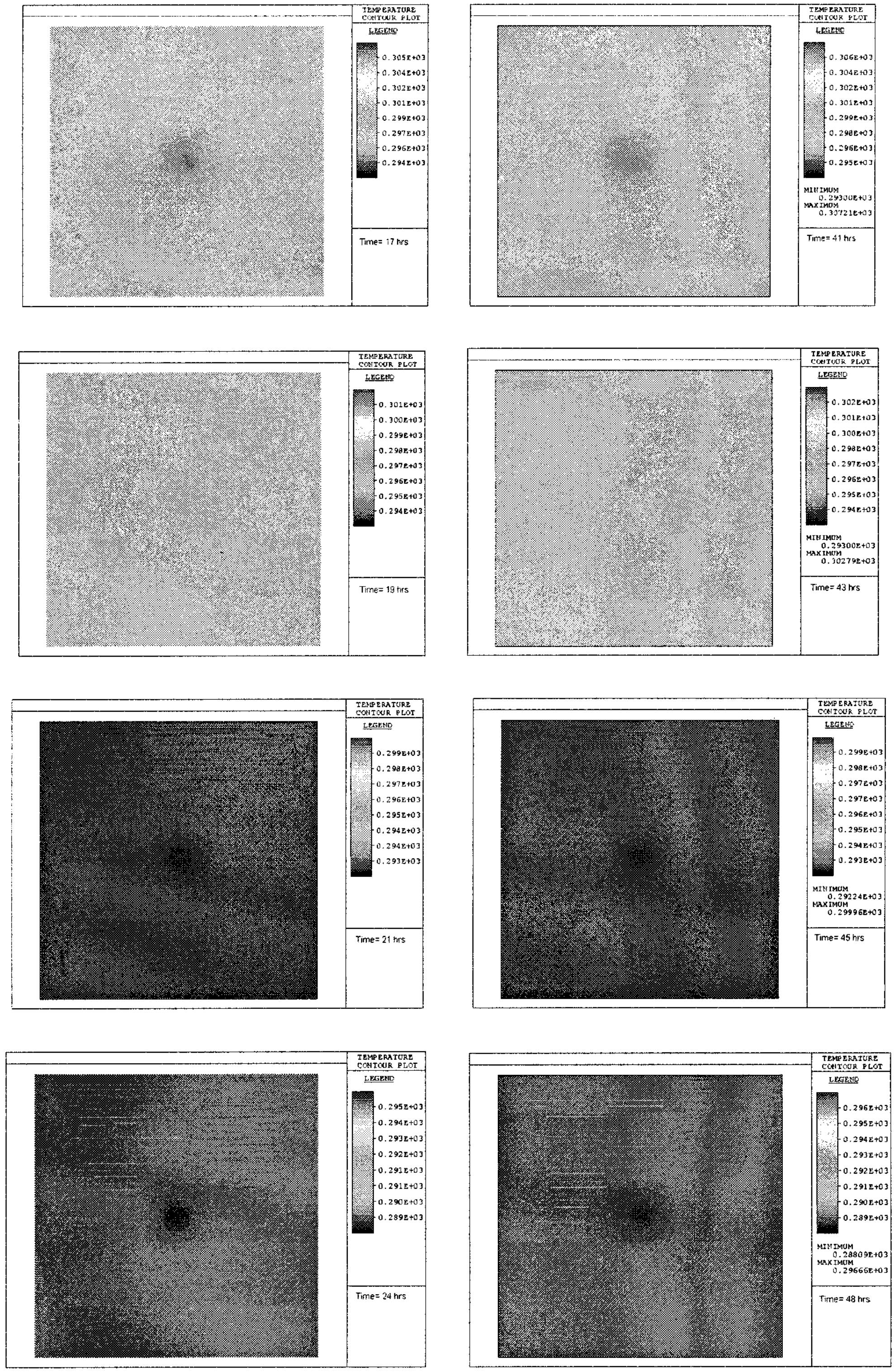

Fig. 8. Periodicity of the soil top surface temperature distribution over the anti-tank simulant buried at 7.6 cm beneath a large-scale clutter surface for $t = 17$, 19, 21, and 24 h, respectively.

symmetric emplacement of the insert within the mine. It can be seen from Fig. 6 that the mine tends to block the conductive heat transfer through the soil beneath the mine until dawn where the effect of the short-wavelength sun radiation is negligible. For later times, the soil top surface temperature rises due to the effect of the incident sun radiation on the soil surface and consequently, more heat is transferred by conduction into the soil layer above the mine. This effect continues up to 3 h from noon. Thereafter, the mine acts as a heat sink till sunset at which time it starts to transfer heat downward by conduction through the soil during the night while the soil temperature above the mine cools promptly due to the effect of radiation from the soil

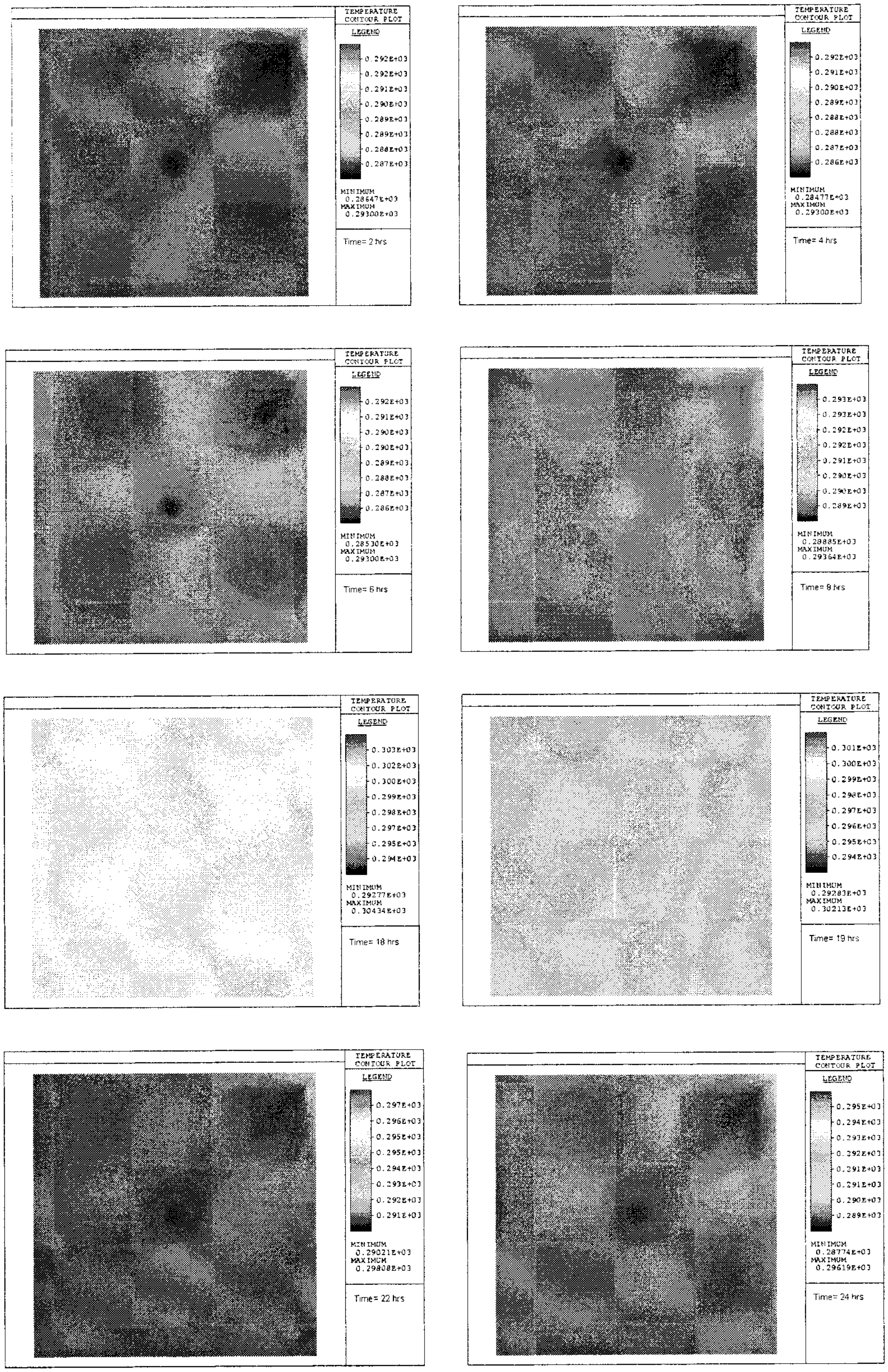

Fig. 9. Effect of the presence of the mine on the top surface temperature of the moderate scale clutter surface at various times.

top surface. This process repeats the same sequence of events for the second diurnal cycle and this can be attributed to the fact that the results become independent after some time following an initial period (e.g., 12 : 36 h, 18 : 42 h, and 24 : 48 h).

This is clearly shown in Figs. 7 and 8. These two figures establish the periodicity of landmine signatures at different time junctures. It can be seen clearly that the temperature pattern repeats itself over a diurnal cycle. Fig. 7 displays in detail the identical nature of the depth-wise temperature distribution over a diurnal cycle (e.g., 12 : 36 h, 18 : 42 h, and 21 : 45 h). In addition, the mine signature at the soil top surface repeats itself every diurnal cycle. The reason for the existence of this periodicity is

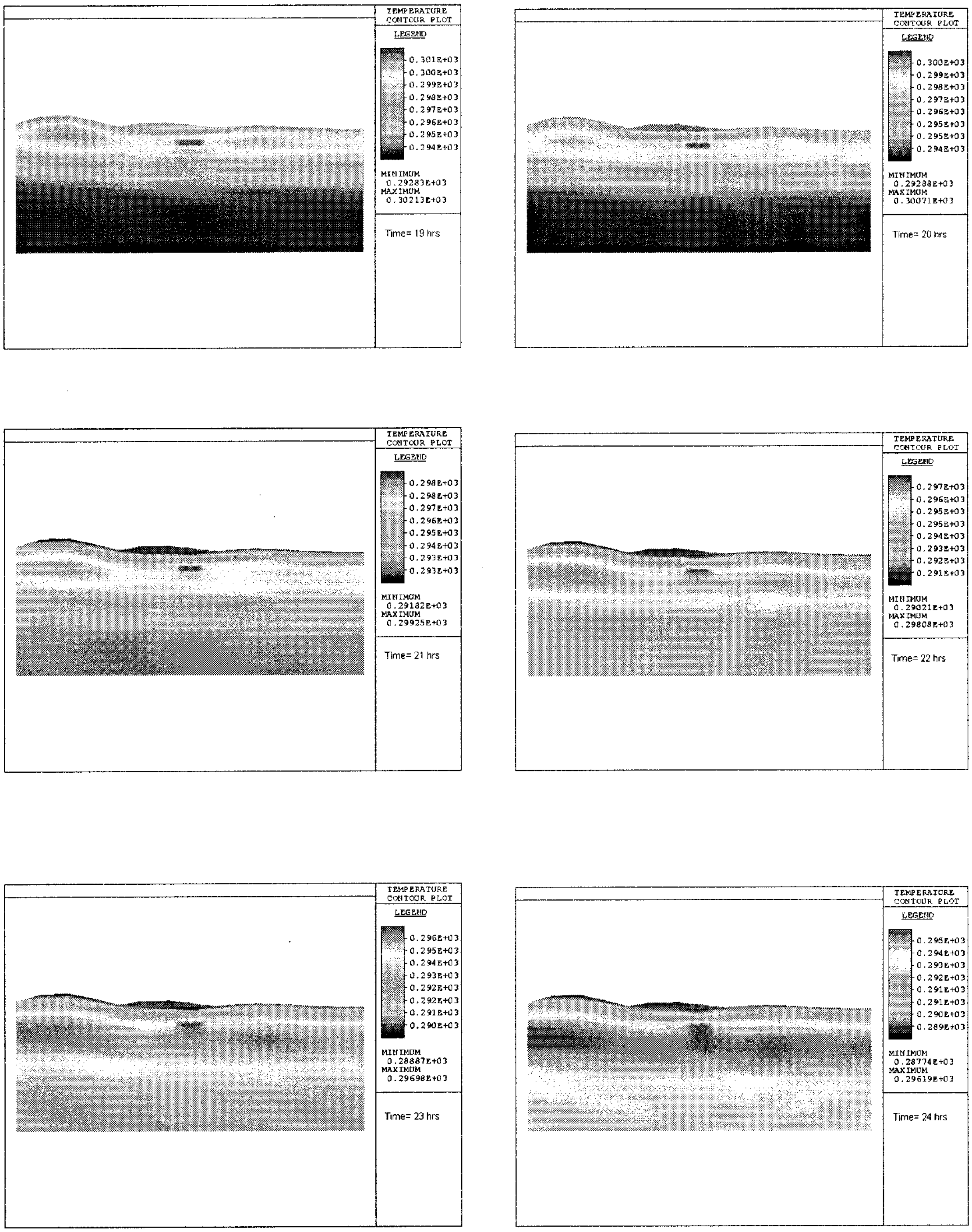

Fig. 10. Depth-wise temperature distribution along a plane (B–B) taken diagonally of a moderate scale clutter surface at various times.

due to the fact that the transient effects die out after the passage of an initial period, which is typically of the order of 12 h.

An interesting situation observed in Fig. 8, demonstrates (Time $= 19$ h) that the mine signature on the soil surface vanishes due to the convergence of the soil surface and the ambient temperatures as depicted in Fig. 4. In order to predict the time at which the signature disappears, the temporal information of the landmine signature on the soil top surface is necessary to resolve this critical time line.

The effect of a buried landmine on the soil surface temperature for moderate-scale clutter surface is shown in Fig. 9. The mine is centered in the middle of the field for this investigation. Fig. 9 shows that the signature pattern changes substantially with time. After midnight (Time ≤ 6 h), the mine is at a relatively cooler temperature and as the time advances, the top surface contrast changes rapidly due to the short-wavelength solar influx ($7 \leq$ Time ≤ 17 h). The signature disappears around the same time (Time $= 19$ h) as in the case of large-scale clutter. In order to capture the mine at that critical period of time, the temporal surface signature will provide the necessary information regarding the location of the mine. This can be accomplished by sweeping the mine site using an IR technique

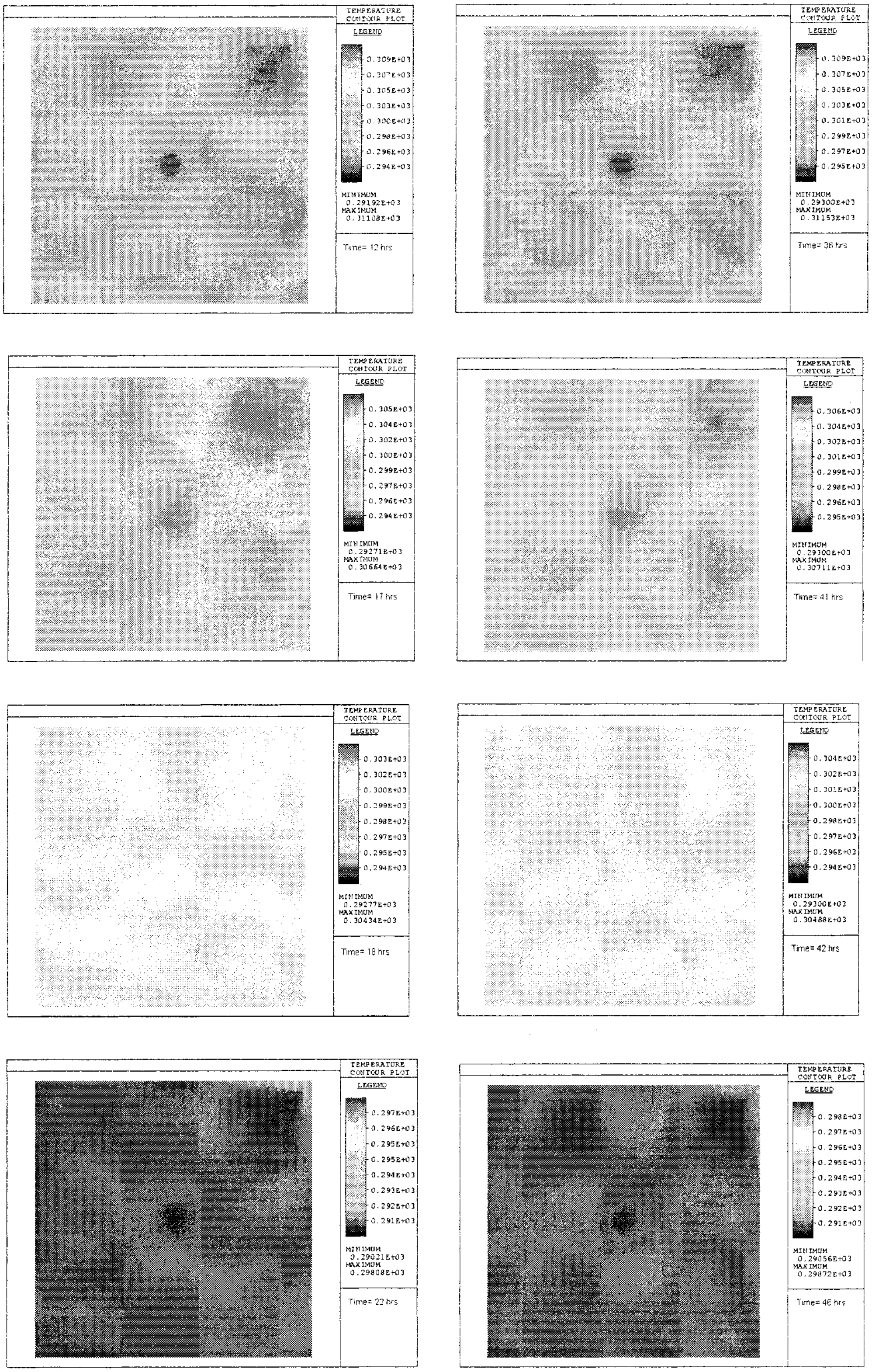

Fig. 11. Periodicity of the soil top surface temperature distribution over the anti-tank simulant buried at 7.6 cm beneath a moderate-scale clutter surface for t = 12, 17, 18, and 22 h, respectively.

at different periods of time where the mine signature does not exist. This is confirmed in Figs. 8 and 9 where the signature of the mine appears again after few hours (Time = 21 h) from the critical period of time at which the signature vanishes (Time = 19 h).

The target of any mine detection method is to achieve a high probability of detection while at the same time maintaining a low probability of false alarm. Thus, reducing the false alarm rate is of immediate importance. Fig. 9 demonstrates that there are other distinguished spots on the top surface of the soil other

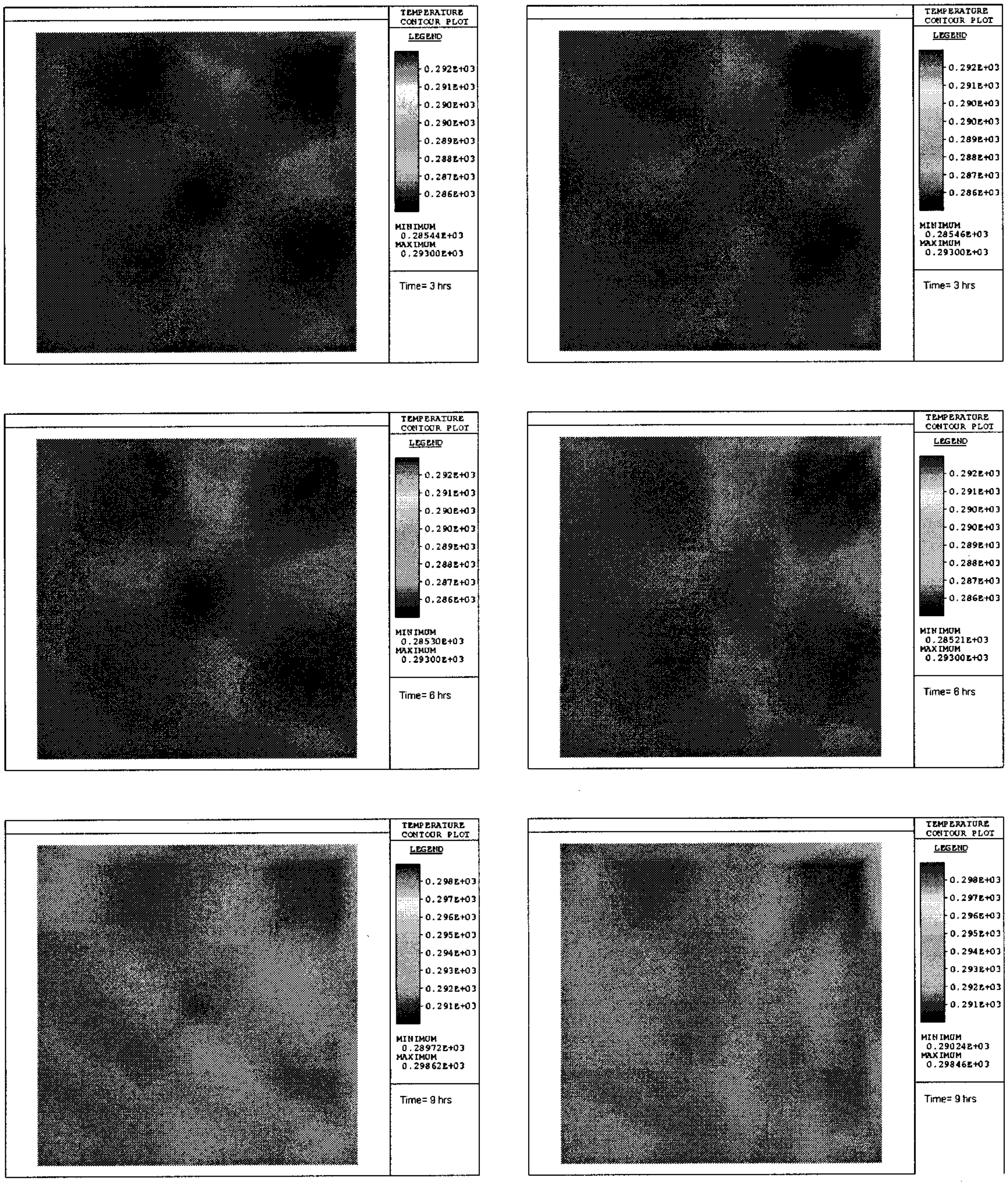

Fig. 12. Comparison of the mine signature on the soil top surface between shallow and moderate depth mine for (a) depth = 7.6 cm and (b) depth = 15.2 cm.

than the mine locations. These spots represent false alarm mine locations as the real mine is located at the center of the soil. Consequently, a simple snap-shot at a given time can provide a false reading. Fig. 10 illustrates the depth-wise temperature distribution taken over a diagonal cut B–B as shown Fig. 3(b) within the mine's field at various periods of time. This plane passes through the center of the mine and two false alarm spots. It is evident from Fig. 10 that only one object is buried beneath the top surface of the soil. To avoid a false reading incidence, the temporal signature pattern of the mine over a number of snap shots in time is necessary to detect the buried landmine.

The periodicity of the soil top surface temperature distribution of an anti-tank mine buried beneath a moderate scale clutter surface is also investigated in this study as shown in Fig. 11. It is clearly seen in this figure that the moderate scale clutter surface establishes periodicity at the same times as that of large-scale clutter surface. The effect of soil depth at which the mine is buried is studied in this analysis. Fig. 12 shows a comparison of the mine signature on the top surface of the soil for the case of moderate scale clutter between shallow and moderate depths of mines buried at various times. Fig. 12 shows that the intensity of the mine's signature deteriorates as the depth at which the mine is buried increases. The mine's signature contrast is more pronounced for shallower buried mines as depicted in Fig. 12. This is due to the more pronounced heat transfer interaction between the mine and the soil's top surface in case of shallow depth buried mines.

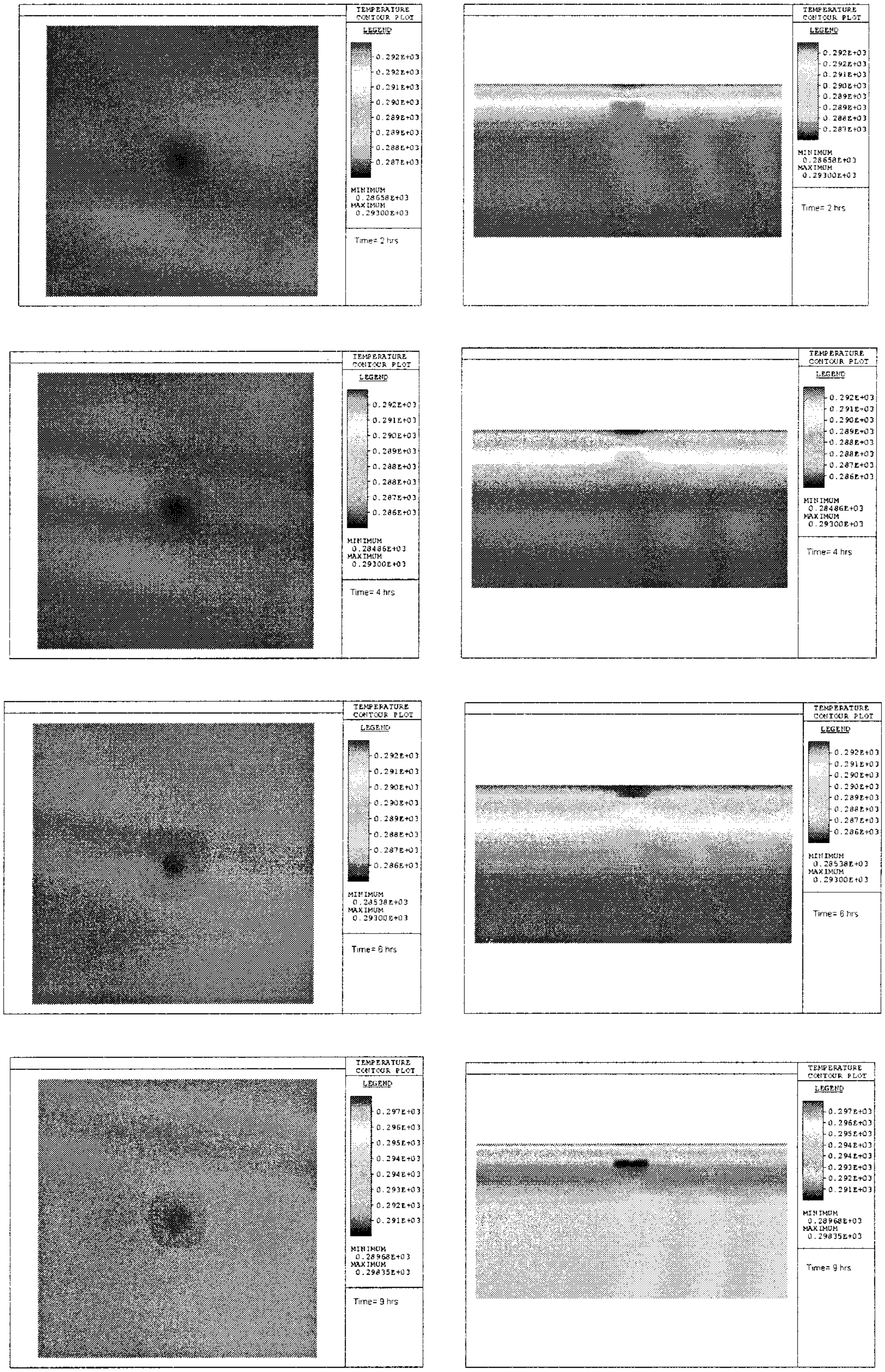

Fig. 13. Effect of the presence of the mine on the soil top surface temperature and the depth-wise temperature distribution (plane A–A) of a smooth surface.

Finally, the effect of the buried landmine on the soil's top surface temperature and the depth-wise temperature distribution for a site with a smooth top surface is shown in Fig. 13. For brevity, only a portion of the results will be presented for this case. It is evident from this figure that the temperature of the soil above the mine is lower than the temperature of the soil underneath the buried mine until dawn. This is associated with the significant effect of the long-wavelength radiation loss into the sky, which overwhelms the effect of the short-wavelength absorbed solar energy during this period of time. As the time advances (Time = 9 h), the surface temperature of the soil rises to a higher temperature due to the effect of the incident solar energy. As a result, the temperature of the soil above the mine becomes greater than the soil temperature beneath the mine. This can be attributed to the effect of heat conduction through the soil.

The effect of the mine on the soil top surface temperature is shown in this figure. It is seen that the mine is clearly recognizable at the center of the field for various time periods. Moreover, Figs. 8, 9, and 13 show that the large-scale and moderate-scale clutter surfaces do produce a significantly different IR signature as compared to a smooth top surface. Consequently, without additional information, the results of a smooth surface model will not be able to properly display the occurrence of false alarms when surface variations are present.

V. Conclusions

The present investigation shows the effect of buried mines on the mine signature and the temperature variations for a smooth, large-scale clutter, and moderate-scale clutter surfaces. The present 3-D investigations describe several new features of the buried objects on the thermal signature of the soil. Generic large scale and moderate scale clutter surfaces are utilized to analyze the effect of surface variation on the mine's signature. The occurrence of false readings is established and the importance of temporal signature snapshots in preventing such readings is discussed. The shallow depth mine is found to produce a more pronounced signature.

References

[1] L. A. LeSchack and N. K. Del Grande, "A dual-wavelength thermal infrared scanner as a potential airborne geophysical exploration tool," *Geophys.*, vol. 41, pp. 1318–1336, 1976.

[2] Y. H. Janssen, A. N. Jong, H. Winkel, and F. J. Putten, "Detection of surface laid and buried mines with IR and CCD cameras, an evaluation based on measurements," *Proc. SPIE*, vol. 2765, pp. 448–459, Apr. 1996.

[3] G. Maksymomko, B. Ware, and D. Poole, "A characterization of diurnal and environmental effects on mines and the factors influencing the performance of mine detecting ATR algorithms," *Proc. SPIE*, vol. 2496, pp. 140–151, Apr. 1995.

[4] J. R. Simard, "Improved landmine detection capability (ILDC): Systematic approach to the detection of buried mines using passive IR imaging," *Proc. SPIE*, vol. 2765, pp. 489–500, Apr. 1996.

[5] B. A. Barbour, M. W. Jones, H. B. Barnes, and C. P. Lewis, "Passive IR polarization sensors: A new technology for mine detection," *Proc. SPIE*, vol. 3392, pp. 96–103, 1996.

[6] M. Larive, L. Collot, S. Breugnot, H. Botma, and P. Roos, "Laid and flush-buried mines (sic) detection using 8-12 μm polarimetric imager," *Proc. SPIE*, vol. 3392, pp. 115–120, 1996.

[7] M. Larive, D. Spoliansky, and O. Trezieres, "Pre-processing of 8–12 μm polarimetric features for laid and flush-buried mines detection," *Proc. SPIE*, vol. 3710, no. 1, pp. 197–202, Apr. 1999.

[8] C. DiMarzio, T. Vo-Dinh, and H. E. Scott, "Some approaches to infrared spectroscopy for detection of buried objects," *Proc. SPIE*, vol. 3392, pp. 158–166, 1996.

[9] A. Filippidis, L. C. Jain, and N. Martin, "Using genetic algorithms and neural networks for surface land mine detection," *IEEE Trans. Signal Procesing*, vol. 47, pp. 176–186, Jan. 1999.

[10] N. K. Del Grande, K. W. Dolan, P. F. Durbin, M. R. Gorvad, B. T. Kornblum, D. E. Perkins, D. J. Schneberk, and A. B. Shapiro, "Three-dimensional thermal imaging of structural flaws by dual-band infrared computed tomography," *Proc. SPIE*, vol. 1942, pp. 207–215, Apr. 1993.

[11] J. Hermann and I. Chant, "Microwave enhancement of thermal landmine signatures," *Proc. SPIE*, vol. 3710, no. 1, pp. 154–166, 1999.

[12] R. Mitchell, S. Somu, and S. Agarwal, "Detection of antipersonnel landmines based on waterjet-induced thermal images," *Proc. SPIE*, vol. 3710, no. 1, pp. 180–188, 1999.

[13] K. Watson, "Geologic applications of thermal infrared images," *Proc. IEEE*, pp. 128–137, Jan. 1975.

[14] H. S. Carslaw and J. C. Yaeger, *Conduction of Heat in Solids*. New York: Oxford Univ. Press, 1953.

[15] A. W. England, "Radiobrightness of diurnally heated, freezing soil," *IEEE Trans. Geosci. Remote Sensing*, vol. 28, pp. 464–475, Apr. 1990.

[16] A. W. England, J. F. Galantowicz, and M. S. Schretter, "The radiobrightness thermal interia measure of soil moisture," *IEEE Trans. Geosci. Remote Sensing*, vol. 30, pp. 132–139, Jan. 1992.

[17] Y. A. Liou and A. W. England, "Annual temperature and radiobrightness signatures for bare soils," *IEEE Trans. Geosci. Remote Sensing*, vol. 34, pp. 981–990, July 1996.

[18] B. A. Baertlin, K. Khanafer, and K. Vafai, "Analysis and modeling of thermal IR signatures of buried land mines," in *Proc. ASC 4th Annu. Conf.*, 2000.

[19] C. W. Allen, *Astrophysical Quantities*. London, U.K.: Athlone , 1963, p. 127.

[20] *FIDAP Theoretical Manual*. Evanston, IL: Fluid Dynamics Int., 1990.

Khalil Khanafer received the B.S. degree in mechanical engineering in 1993 and the M.Sc. degree in mechanical engineering in 1997 from Kuwait University, Kuwait. He is currently pursuing the Ph.D degree with the Department of Mechanical Engineering at The Ohio State University (OSU), Columbus.

Since 1998, he has been a Graduate Research Associate at OSU. His interests include fluid flow and heat transfer in porous medium, cooling of electronic equipment, natural convection in open-ended enclosures, and nanotechnology.

Kambiz Vafai received the B.S. in mechanical engineering from the University of Minnesota, Minneapolis, in 1975. He received the M.S. degree in mechanical engineering and the Ph.D. degree in mechanical engineering from the University of California, Berkeley, in 1977 and 1980, respectively.

He is the holder of the Presidential Chair at the University of California, Riverside, and has been the Editor-in-Chief of *Journal of Porous Media* since 1997. Also, he is on the editorial advisory boards of several international journals in the field of heat and mass transfer. His current research interests include transport through porous media, multiphase transport, natural convection in complex configurations, analysis of porous insulations, heat flux applications, free surface flows, flat-shaped heat pipes, and power electronics. He has conducted basic and applied research in several areas related to heat and mass transfer, such as fundamental aspects of transport through porous media, natural convection in open-ended configurations, condensation and phase change, multiphase transport through porous media, and flow and heat transfer in the brake housing of an aircraft.

Dr. Vafai has won various awards and been an invited professor at universities in France, Germany, and Italy. He is a Fellow of American Society of Mechanical Engineers since 1992 and has been an Associate Fellow of American Institute of Aeronautics and Astronautics since 1998.